Journal of Geophysical Research: Earth Surface

RESEARCH ARTICLE
10.1029/2018JF004616

The Influence of Storms on Sand Wave Evolution: A Nonlinear Idealized Modeling Approach

G. H. P. Campmans[1], **P. C. Roos**[1], **H. J. de Vriend**[1], **and S. J. M. H. Hulscher**[1]

[1]Water Engineering and Management, University of Twente, Enschede, The Netherlands

Key Points:
- We present a new 2DV nonlinear morphodynamic model to study sand wave evolution toward equilibrium
- Model runs show that steady wind-driven flow and wind wave conditions decrease equilibrium height
- Intermittent storms give a dynamic equilibrium, significantly lower already for short storm duration

Correspondence to:
G. H. P. Campmans,
g.h.p.campmans@utwente.nl

Citation:
Campmans, G. H. P., Roos, P. C., de Vriend, H. J., & Hulscher, S. J. M. H. (2018). The influence of storms on sand wave evolution: A nonlinear idealized modeling approach. *Journal of Geophysical Research: Earth Surface*, *123*, 2070–2086. https://doi.org/10.1029/2018JF004616

Received 1 FEB 2018
Accepted 15 JUL 2018
Accepted article online 2 AUG 2018
Published online 7 SEP 2018

Abstract We present a new 2DV nonlinear process-based morphodynamic model to investigate the effects of storms, specifically wind-driven flow and wind waves, on finite amplitude tidal sand wave evolution. Simulations are performed on periodic domains of two lengths: (i) on a 350-m domain, comparable to the wavelength of observed sand waves, we study the evolution toward equilibrium shapes, and (ii) on a 4-km domain, we study the evolution from a randomly perturbed seabed. Our model results demonstrate that both wind-driven flow and wind waves reduce sand wave height and tend to increase wavelength. Wind-driven flow breaks the tidal symmetry, resulting in horizontal sand wave asymmetry and migration. Waves alone do not induce migration but can enhance migration induced by, for example, tidal asymmetry and wind-driven flow. On the 350-m domain, we further find that migration rates decrease with increasing sand wave height. However, in an irregular sand wave field, large sand waves tend to overtake the smaller ones, suggesting a complicated interaction among neighboring bed forms. The above results concern steady state storm conditions. However, since storms occur on an intermittent basis, we also simulated a synthetic storm climate consisting of alternating short periods of storm conditions and long periods of fair-weather conditions. Simulations reveal a dynamic equilibrium with sand wave heights significantly below those obtained for tide-only conditions, also for relatively short storm duration. Our work identifies mechanisms that explain why sand wave heights are generally overpredicted by numerical models that do not include storm processes.

1. Introduction

In many tidally dominated shallow seas, tidal sand waves are observed, where typical water depths are 15–50 m (Hulscher & van den Brink, 2001). Sand waves are large-scale dynamic bed forms that form a rhythmic seabed pattern (e.g., McCave, 1971; Terwindt, 1971). They have heights of several meters and wavelengths of 100–1,000 m, can migrate up to several meters per year (Damen et al., 2018; Van Dijk & Kleinhans, 2005), and are typically formed at the time scales of several years.

The presence of sand waves dynamically affects the seabed topography, thus posing danger to navigation (Dorst et al., 2011), burying and exposing objects at the seabed such as sea mines and ship wrecks, creating free spans of cables and pipelines, and affecting stability of offshore structures such as pylons for wind turbines and platforms. For all of these applications, an accurate understanding of seabed dynamics and thus sand wave dynamics is desirable.

Even though tidal sand waves are generally believed to be formed and shaped by tidal currents, observational studies have shown that storm processes decrease their height (Houthuys et al., 1994; Terwindt, 1971; Van Dijk & Kleinhans, 2005) and significantly affect migration speed and direction (Fenster et al., 1990; Harris, 1989; Le Bot et al., 2000). Below we describe the literature on sand wave modeling, particularly focusing on the influence of storms.

Process-based models have been developed to understand the processes behind sand wave dynamics (see, e.g., the review by Besio et al., 2008). Using a linear stability analysis, tidal sand waves have been explained as an instability of a sandy seabed subject to tidal flow (Hulscher, 1996). Tidally averaged recirculation cells tend to move sediment toward the crest, whereas gravity favors downslope transport toward the troughs. The perturbation with the largest growth rate is termed the fastest growing mode (FGM) and is considered to be the preferred bed form (Dodd et al., 2003).

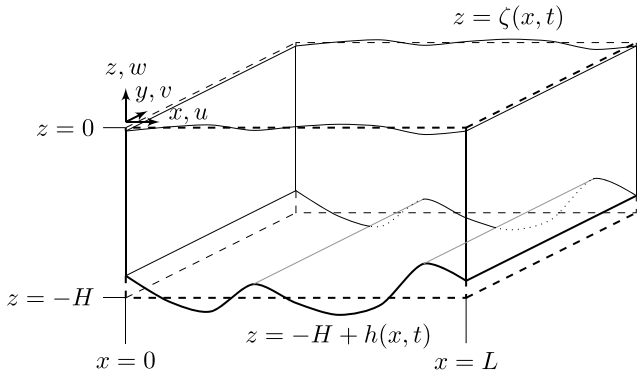

Figure 1. The model domain, a 2DV model, that allows for velocity components but no variations in the *y* directions: $\partial/\partial y(\cdot) = 0$. In the *x* direction, the domain is spatially periodic, with a domain length *L*.

Later, other researchers extended this linear stability approach to investigate the effect of various physical mechanisms on sand wave dynamics. For example, sand wave migration can be caused by pressure-gradient or wind-driven flow (Németh et al., 2002) or by tidal asymmetry (Besio et al., 2004). Others investigated the effect of a refined turbulence model (Blondeaux & Vittori, 2005a, 2005b; Borsje et al., 2014) and grain-size variation (Roos et al., 2007; Van Oyen & Blondeaux, 2009). Campmans et al. (2017) investigated the effects of storms, wind waves, and wind-driven flow on sand wave formation using linear stability analysis of an idealized sand wave model. They concluded that storm effects indeed affect sand waves in the small amplitude regime. Wind waves and wind-driven flow decrease the growth rate and increase the preferred wavelength of sand waves. Wind waves may enhance migration due to other processes, such as wind-driven flow, residual tidal current, or tidal asymmetry. Importantly, these studies are limited to small amplitude seabed topographies only.

Nonlinear models were developed in order to explain finite amplitude sand wave behavior. Németh et al. (2007) investigated sand wave height, shape, and migration. Van den Berg et al. (2012) developed a sand wave solution method based on a spectral time-integration method for the flow, in order to investigate sand wave variation on large model domains. Later, a case study compared an initial version of this model with field data (Sterlini et al., 2009). All of these studies were able to describe equilibrium sand wave profiles on a domain with a length in the order of hundreds of meters. Shortcomings of these type of models are generally that the sand wave height is significantly overpredicted with sand wave heights in the order of 10 m instead of several meters and that the wavelength keeps increasing for larger model domains.

From the above literature review, we conclude that (i) the influence of storms on sand wave dynamics is significant but has been modeled in the linear regime only and that (ii) nonlinear models suffer from various shortcomings, such as overpredicting sand wave height. Therefore, the goal of this study is to assess the influence of storm processes on sand wave dynamics in the finite amplitude regime. Specifically, we address the following research questions. Do storm effects lead to a decrease in sand wave height, and how do they affect sand wave shape and migration speeds?

To that end, we numerically solve the shallow water equations on a 2DV periodic domain, where tidal and wind-driven flows—enhanced by wave stirring—trigger sediment transport. With this model, we systematically investigate the effect of wind-driven flow and wind waves on the evolution and final sand wave characteristics. We use simulations on both short and long domains with spatially periodic boundary conditions, because a short domain artificially fixes the wavelength as mentioned by Van den Berg et al. (2012). This would exclude the investigation of nonlinear wavelength effects.

The paper is structured as follows. Section 2 gives the model formulation, and section 3 describes the solution procedure. In section 4, finite amplitude model results are shown. Finally, sections 5 and 6 contain the discussion and conclusions, respectively.

2. Model Formulation

2.1. Geometry

The model domain is schematically shown in Figure 1. It is a two-dimensional (x, z) domain, in which flow is allowed in the third dimension. However, no variations in the *y* directions are allowed $\partial/\partial y(\cdot) = 0$. Including flow in the second horizontal dimension allows for arbitrary wind and wave angles. The domain is spatially periodic in the *x* direction, with domain length *L*, the mean water depth is *H*, with an undulating seabed topography *h*, and surface elevation ζ which are both functions of *x* and *t*. Horizontally integrated, the seabed topography and surface elevation are zero, that is, $\int_0^L h\mathrm{d}x = 0$ and $\int_0^L \zeta \mathrm{d}x = 0$. The tidal flow is directed parallel to the *x* axis, whereas wind waves and wind may be directed under an angle with respect to the *x* axis (Figure 2). Spatial periodicity implies that all quantities (and their derivatives) are the same at $x = 0$ and $x = L$.

2.2. Hydrodynamics

The pressure is assumed to be in hydrostatic balance, so that the continuity and momentum equations in the original (x, z) domain are given by

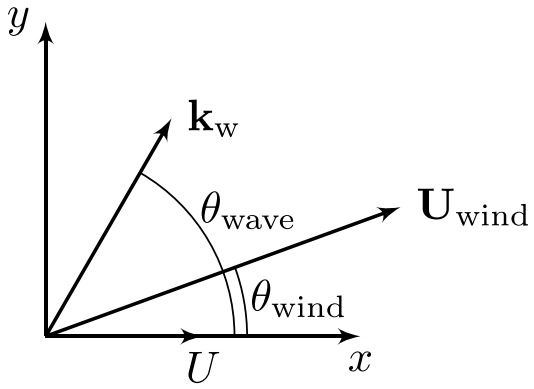

Figure 2. Definition sketch (top view) of the tidal current U, the wind velocity vector $\mathbf{U}_{wind}$, and wave vector $\mathbf{k}_w$ (in the direction in which the waves propagate). Although the depth-averaged tidal flow can be in arbitrary direction, in our model simulations it is always chosen aligned with the x axis.

$$\nabla \cdot \mathbf{u} = 0, \tag{1}$$

$$\frac{\partial \mathbf{u}_h}{\partial t} + \mathbf{u} \cdot \nabla \mathbf{u}_h + g \nabla_h \zeta + \mathbf{F} - \frac{\partial}{\partial z}\left(A_v \frac{\partial \mathbf{u}_h}{\partial z}\right) = 0. \tag{2}$$

Here $\mathbf{u} = (u, v, w)^T$ is the velocity vector in the Cartesian coordinates $\mathbf{x} = (x, y, z)^T$, subscript h denotes the horizontal (x and y) components of the vector, g is the gravitational acceleration constant, ζ is the free surface elevation response to seabed undulations, and $\mathbf{F} = (F_x, 0)^T$ is a spatially uniform forcing term representing free surface elevation gradient of the tidal wave. Turbulence is represented using the combination of a constant vertical eddy viscosity A_v (Bowden et al., 1959) and a partial slip condition at the bed (e.g., Campmans et al., 2017; Hulscher, 1996; Van den Berg et al., 2012). More refined turbulence models such as a Dean profile (Besio et al., 2006) or a k-ε (Borsje et al., 2013) model lead to quantitatively different but not qualitatively different results in the linear regime. The Coriolis effect is neglected, as it is only of minor importance for sand wave dynamics (Hulscher, 1996).

The boundary conditions at the free surface (rigid lid) and the sea bed (partial slip) are given by

$$\begin{aligned} w &= 0, & A_v \frac{\partial \mathbf{u}_h}{\partial z} &= \frac{\boldsymbol{\tau}_{wind}}{\rho}, & &\text{at} \quad z = 0, \\ w &= u\frac{\partial h}{\partial x}, & \frac{\boldsymbol{\tau}}{\rho} &\equiv A_v \frac{\partial \mathbf{u}}{\partial z} = S\mathbf{u}_h, & &\text{at} \quad z = -H + h. \end{aligned} \tag{3}$$

Here $\boldsymbol{\tau}_{wind}$ is the wind-induced shear stress, ρ the density of water, h the sea bed topography, S the slip parameter (Maas & van Haren, 1987), and finally, $\boldsymbol{\tau}$ is the bed shear stresses due to wind-driven and tidal currents. The wind-induced shear stress $\boldsymbol{\tau}_{wind}$ at the sea surface is given by

$$\boldsymbol{\tau}_{wind} = \rho_a C_d |\mathbf{U}_{wind}| \mathbf{U}_{wind}, \tag{4}$$

where $\mathbf{U}_{wind}$ is the horizontal wind velocity vector at 10 m above the sea surface, $C_d = (0.75{+}0.067|\mathbf{U}_{wind}|)10^{-3}$ is a friction factor (Makin et al., 1995), and ρ_a is the air density. The wind vector has a magnitude $|\mathbf{U}_{wind}|$ and an angle θ_{wind} with respect to the x axis (see Figure 2). The forcing term F_x is chosen such that the tidal flow, over a flat bed and in absence of wind-driven flow, satisfies

$$\frac{1}{H}\int_{-H}^{0} \mathbf{u}_h \, dz = [U_{M2}, 0]^T \sin(\sigma_t t), \tag{5}$$

where U_{M2} is the depth-averaged tidal velocity amplitude and σ_t the tidal angular frequency. Note that in equation (5), we have chosen symmetrical tidal flow but additional components could be forced as well.

The waves are monochromatic, with a prescribed period and energy flux component in x direction. Wave kinematics are modeled by linear wave theory (e.g., Mei, 1989), including local and instantaneous adaptation due to shoaling and refraction over the varying water depth. Wave diffraction and wave-current interactions are excluded, the latter because typical wave speeds (~10 m/s) are well above the current speeds (<1 m/s). The total bed shear stress due to both wind waves and the currents is modeled as the sum of the two shear stress contributions due to currents and waves, that is,

$$\boldsymbol{\tau}_{cw} = \boldsymbol{\tau} + \boldsymbol{\tau}_w. \tag{6}$$

Here $\boldsymbol{\tau}$ is as defined in equation (3), whereas the wave-induced bed shear stress is given by

$$\boldsymbol{\tau}_w = \frac{1}{2}\rho f_w |\mathbf{u}_w| \mathbf{u}_w, \tag{7}$$

where f_w is a wave friction factor (Nielsen, 1992), and $\mathbf{u}_w$, the near-bed wave orbital velocity vector, is given by

$$\mathbf{u}_w = \frac{\mathbf{k}_w}{|\mathbf{k}_w|} \frac{\sigma_w H_w \cos(\sigma_w t)}{2\sinh(|\mathbf{k}_w|(H-h))}. \tag{8}$$

Here $\mathbf{k}_w$ is the local wave vector, σ_w the wave angular frequency, and H_w the local wave height. The wave period is given by $T = 2\pi/\sigma_w$. The magnitude of the wave vector $\mathbf{k}_w$ is determined by the dispersion relation

$$\sigma_w^2 = g|\mathbf{k}_w| \tanh(|\mathbf{k}_w|(H-h)), \tag{9}$$

and the wave propagation angle is given by Snell's law:

$$\frac{\sin\theta_{wave}}{c} = \frac{\sin\theta_{wave0}}{c_0}, \tag{10}$$

where the θ_{wave} is defined as the angle between the x axis and the propagation direction of the waves (see Figure 2); the wave celerity is given by $c = \sigma_w/|\mathbf{k}_w|$. The quantities with subscript 0 denote the reference wave conditions, that is, the wave conditions for the waves that would travel through the domain if the seabed were flat. Note that for large reference wave angles, Snell's law in equation (10) produces complex angles in sand wave troughs, which prevents us from using reference wave angles close to 90°. The local wave height H_w is computed from wave energy conservation and reads

$$H_w = \sqrt{\frac{c_{g,0}}{c_g}}\sqrt{\frac{\cos\theta_{wave0}}{\cos\theta_{wave}}}H_{w0}, \tag{11}$$

where the wave group speed c_g is given by

$$c_g = \left[\frac{1}{2} + \frac{|\mathbf{k}_w|(H-h)}{\sinh(2|\mathbf{k}_w|(H-h))}\right]c. \tag{12}$$

2.3. Sediment Transport

Following Hulscher (1996), we consider bed load sediment transport only, which is modeled as a power law of the bed shear stress, including a slope correction term, favoring downhill transport, given by

$$\mathbf{q}_b = \alpha_b|\boldsymbol{\tau}_{cw}|^{\beta_b}\left(\frac{\boldsymbol{\tau}_{cw}}{|\boldsymbol{\tau}_{cw}|} - \lambda\nabla_h h\right). \tag{13}$$

Here $\mathbf{q}_b$ is the sediment transport flux, α_b is the bed load coefficient derived from Van Rijn (1993), β_b the exponent that expresses the nonlinearity of the bed load transport, and λ is the slope correction parameter.

2.4. Bed Evolution

The bed evolution satisfies the Exner equation for sediment conservation

$$(1-p)\frac{\partial h}{\partial t} = -\nabla_h \cdot \langle \mathbf{q}_b \rangle, \tag{14}$$

where p is the bed porosity. Furthermore, $\langle\cdot\rangle$ denotes that we use the wave and tidally averaged sediment flux for seabed evolution, as a scaling analysis (Campmans et al., 2017) has demonstrated that we may consider separation of time scales. In our model, we distinguish between three time scales: first, that of the wind waves (3–10 s); second, that of the tidal current (~12 hr); and third, that of morphodynamic changes (months to years). On the intrawave time scale, the shear stress due to the currents is kept constant, and the sediment transport (equation (13) is evaluated at a number of points in the wave cycle and then averaged over one wind wave period. Likewise, the morphological time scale is much longer than the tidal period; hence, the seabed is kept constant on the hydrodynamic time scale. The sediment flux on the hydrodynamic time scale is then tidally averaged to obtain the bed evolution at the morphological time scale.

3. Solution Method

The morphodynamic model is solved in several steps. First, the hydrodynamic model equations are transformed to a rectangular domain. Second, the hydrodynamic model equations are discretized and numerically integrated over time. Third, the sediment transport is computed. Finally, the seabed evolution is computed.

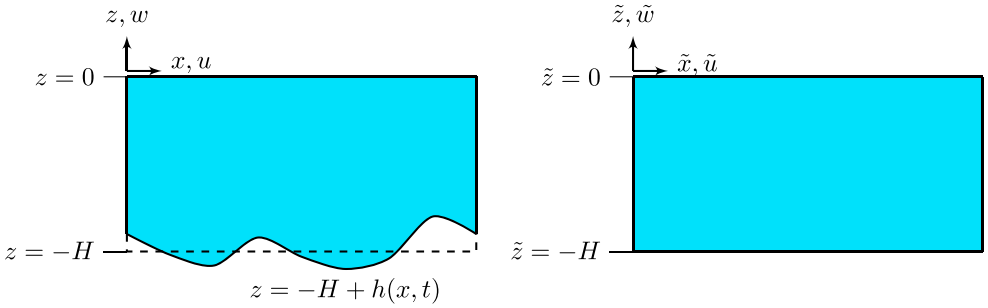

Figure 3. The transformation from the Cartesian (x, z) model domain toward the rectangular $(\tilde{x}, \tilde{z})$ model domain in which the transformed model equations will be solved numerically.

3.1. Coordinate transform

Following Van den Berg et al. (2012), we transform the hydrodynamic model equations from the Cartesian horizontal coordinate x and vertical coordinate z to coordinates $\tilde{x}$ and $\tilde{z}$ such that the transformed domain is rectangular and hence easier to discretize. The coordinate transformation is given by

$$\tilde{x} = x, \qquad \tilde{z} = H\frac{z}{H-h}, \tag{15}$$

and shown in Figure 3. This transformation uniquely maps coordinates to the transformed coordinate set, because the determinant of the transformation Jacobian

$$\mathcal{J} = \frac{\partial(\tilde{x},\tilde{z})}{\partial(x,z)} = \begin{bmatrix} \frac{\partial\tilde{x}}{\partial x} & \frac{\partial\tilde{x}}{\partial z} \\ \frac{\partial\tilde{z}}{\partial x} & \frac{\partial\tilde{z}}{\partial z} \end{bmatrix} = \begin{bmatrix} 1 & 0 \\ \eta & \xi \end{bmatrix}, \tag{16}$$

is nonzero: $\det(\mathcal{J}) = \xi$. Here η and ξ are given by

$$\eta = H\frac{z}{(H-h)^2}\frac{\partial h}{\partial x}, \qquad \xi = \frac{H}{H-h}. \tag{17}$$

After the coordinate transformation, a variable transformation is applied introducing $(\tilde{\mathbf{u}}_\mathrm{h}, \tilde{w})$ such that

$$\mathbf{u}_\mathrm{h} = \xi\tilde{\mathbf{u}}_\mathrm{h}, \qquad w = \tilde{w} - \eta\tilde{u}. \tag{18}$$

This variable transformation enables us to write the hydrodynamic model problem in conservative form:

$$\frac{\partial\tilde{u}}{\partial\tilde{x}} + \frac{\partial\tilde{w}}{\partial\tilde{z}} = 0, \tag{19}$$

$$\frac{\partial\tilde{u}}{\partial t} + \frac{\partial}{\partial\tilde{x}}(\tilde{F}_{u,x}) + \frac{\partial}{\partial\tilde{z}}(\tilde{F}_{u,z}) + \frac{g}{\xi}\frac{\partial\tilde{\zeta}}{\partial\tilde{x}} - \frac{\tilde{F}_x}{\xi} = 0, \tag{20}$$

$$\frac{\partial\tilde{v}}{\partial t} + \frac{\partial}{\partial\tilde{x}}(\tilde{F}_{v,x}) + \frac{\partial}{\partial\tilde{z}}(\tilde{F}_{v,z}) - \frac{\tilde{F}_y}{\xi} = 0, \tag{21}$$

where the fluxes $\tilde{F}$ are given by

$$\begin{aligned} \tilde{F}_{u,x} &= \xi\tilde{u}^2, \\ \tilde{F}_{u,z} &= \xi\tilde{u}\tilde{w} - \xi^2 A_\mathrm{v}\frac{\partial\tilde{u}}{\partial\tilde{z}}, \\ \tilde{F}_{v,x} &= \xi\tilde{v}\tilde{u}, \\ \tilde{F}_{v,z} &= \xi\tilde{v}\tilde{w} - \xi^2 A_\mathrm{v}\frac{\partial\tilde{v}}{\partial\tilde{z}}, \end{aligned} \tag{22}$$

with corresponding transformed boundary conditions given by

$$\begin{aligned} \tilde{w} &= 0, & \xi^2 A_\mathrm{v}\frac{\partial\tilde{\mathbf{u}}_\mathrm{h}}{\partial\tilde{z}} &= \frac{\boldsymbol{\tau}_\mathrm{wind}}{\rho}, & \text{at} \quad \tilde{z} &= 0, \\ \tilde{w} &= 0, & \frac{\boldsymbol{\tau}}{\rho} \equiv \xi^2 A_\mathrm{v}\frac{\partial\tilde{\mathbf{u}}_\mathrm{h}}{\partial\tilde{z}} &= \xi S\tilde{\mathbf{u}}_\mathrm{h}, & \text{at} \quad \tilde{z} &= -H. \end{aligned} \tag{23}$$

Note that $\eta = 0$ at $\tilde{z} = 0$ and $\eta = \xi\frac{\partial h}{\partial x}$ at $\tilde{z} = -H$.

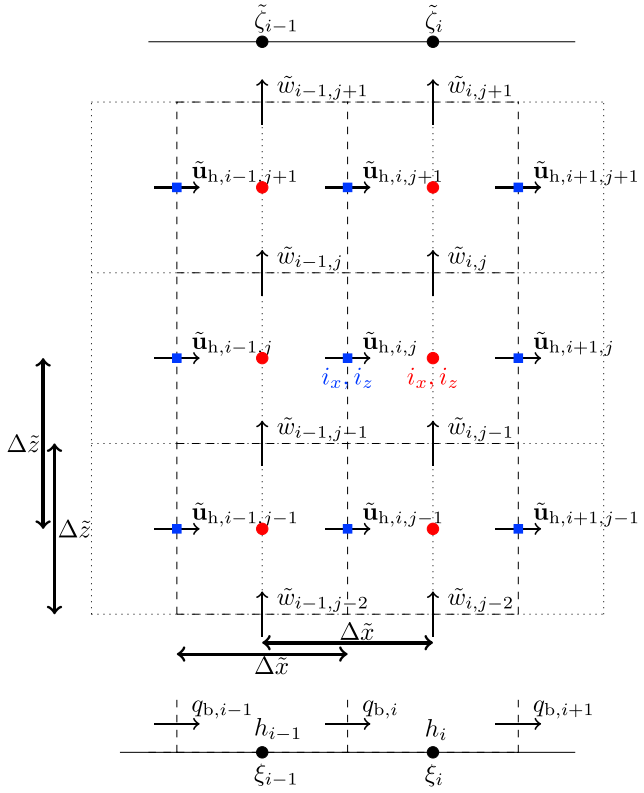

Figure 4. The unknowns $\tilde{\mathbf{u}}_{\mathrm{h}} = (\tilde{u}, \tilde{v})^T$ and $\tilde{w}$ are discretized in the model domain using a staggered grid. The red circles indicate locations where the discrete continuity equations are evaluated, and the blue squares indicate the locations where the discrete momentum equations are evaluated. The grid spacing is equidistant with $\Delta\tilde{x}$ and $\Delta\tilde{z}$ spacing in the horizontal and vertical direction, respectively.

3.2. Discretization

3.2.1. Hydrodynamics

The transformed hydrodynamic model problem is discretized using a finite difference method on a staggered grid, shown in Figure 4, where discrete horizontal velocities $\tilde{\mathbf{u}}_{\mathrm{h},i,j} = (\tilde{u}_{i,j}, \tilde{v}_{i,j})^T$ are defined at points $[\tilde{x}_i, \tilde{z}_j] = [(i-1)\Delta\tilde{x}, (j-\frac{1}{2})\Delta\tilde{z} - H]$ for $[1 \le i \le I, 1 \le j \le J]$ and discrete vertical velocities $\tilde{w}_{i,j}$ are defined at points $[\tilde{x}_i, \tilde{z}_j] = [(i-\frac{1}{2})\Delta\tilde{x}, j\Delta\tilde{z} - H]$ for $[1 \le i \le I, 1 \le j \le J+1]$. Here $\Delta\tilde{x}$ and $\Delta\tilde{z}$ are the uniform step sizes in $\tilde{x}$ and $\tilde{z}$ directions, and I and J are the number of discrete points in $\tilde{x}$ and $\tilde{z}$ directions, respectively. The spatial discretization of the hydrodynamics is given in Appendix A. The corresponding temporal integration is performed by forward Euler, in which the surface elevation is iteratively solved such that the continuity equation and the vertical velocity boundary conditions are fulfilled, as well as the conservation of ζ over the domain. For the hydrodynamic time integration, we use an adaptive step size Δt_{hyd}, such that $\Delta t_{\mathrm{hyd}} \le 0.35/(\tilde{u}\tilde{\xi}/\Delta\tilde{x} + \tilde{w}\tilde{\xi}/\Delta\tilde{z})$ in each morphodynamic time step.

3.2.2. Sediment Transport

The instantaneous discrete sediment flux in the x direction is given by

$$q_{\mathrm{b},x,i} = \alpha_{\mathrm{b}} |\boldsymbol{\tau}_{\mathrm{cw},i}|^{\beta_{\mathrm{b}}} \left(\frac{\tau_{\mathrm{cw},x,i}}{|\boldsymbol{\tau}_{\mathrm{cw},i}|} - \lambda \frac{h_i - h_{i-1}}{\Delta x} \right), \tag{24}$$

where $\boldsymbol{\tau}_{\mathrm{cw},i}$ includes the spatially varying wave-induced shear stress. The wind wave (64 points) and tidally averaged (typically 30,000 points) sediment flux is then used for the seabed evolution. To separately investigate the influence of the flow-induced and the slope-induced sediment transport on the sand wave evolution, we write $q_{\mathrm{b},x,i} = q_{\mathrm{b},x,i,\mathrm{fe}} + q_{\mathrm{b},x,i,\mathrm{se}}$ with

$$q_{\mathrm{b},x,i,\mathrm{fe}} = \alpha_{\mathrm{b}} |\boldsymbol{\tau}_{\mathrm{cw},i}|^{\beta_{\mathrm{b}}} \frac{\tau_{\mathrm{cw},x,i}}{|\boldsymbol{\tau}_{\mathrm{cw},i}|} \quad \text{and} \quad q_{\mathrm{b},x,i,\mathrm{se}} = -\lambda\alpha_{\mathrm{b}} |\boldsymbol{\tau}_{\mathrm{cw},i}|^{\beta_{\mathrm{b}}} \frac{h_i - h_{i-1}}{\Delta x}, \tag{25}$$

respectively.

Table 1
The Parameter Settings Used for the Various Model Runs

Description	Symbol	Typical value	Unit
Tidal velocity amplitude	U_{M2}	0.5	m/s
Tidal angular frequency	σ_t	$1.41 \cdot 10^{-4}$	rad/s
Vertical eddy viscosity	A_v	0.04	m^2/s
Slip parameter	S	0.01	m/s
Bed porosity	p	0.4	-
Gravitational acceleration	g	9.81	m/s^2
Water density	ρ	1,020	kg/m^3
Air density	ρ_a	1.225	kg/m^3
Wave friction factor	f_w	0.1	-
Mean water depth	H	30	m
Bed load coefficient	α_b	$1.56 \cdot 10^{-5}$	$m^{\beta_b+2} \cdot s^{2\beta_b-1} \cdot kg^{-\beta_b}$
Bed load exponent	β_b	1.5	-
Slope correction parameter	λ	1.5	-

3.3. Bed Evolution

The bed evolution equation (14) is discretized by using a semi-implicit scheme

$$(1-p)\frac{h_i^{n+1}-h_i^n}{\Delta t_{mor}} = -\left[\frac{\langle q^n_{b,x,i+1,fe}\rangle - \langle q^n_{b,x,i,fe}\rangle}{\Delta x} - \alpha_b\lambda\frac{\langle|\boldsymbol{\tau}^n_{cw,i+1}|^{\beta_b}\rangle\left[\frac{h^n_{i+1}-h^n_i}{2\Delta x}+\frac{h^{n+1}_{i+1}-h^{n+1}_i}{2\Delta x}\right]-\langle|\boldsymbol{\tau}^n_{cw,i}|^{\beta_b}\rangle\left[\frac{h^n_i-h^n_{i-1}}{2\Delta x}+\frac{h^{n+1}_i-h^{n+1}_{i-1}}{2\Delta x}\right]}{\Delta x}\right], \quad (26)$$

where time is discretized by $t_n = n\Delta t_{mor}$, and the two terms in the bed load transport formula (24) are treated separately. The bed shear stress is explicit in this scheme, whereas the seabed gradient is discretized using an implicit Crank-Nicolson type of approach. This implicit scheme provides stability of the slope effect for larger morphodynamic time steps compared to those in a fully explicit scheme. The morphodynamic time step Δt_{mor} typically ranges from a week to month. Finally, the conservative flux formulation in equation (26) guarantees conservation of sediment.

4. Results

We first compare the nonlinear sand wave model with the linear stability analysis for small amplitude sand waves (section 4.1). Next, we investigate the evolution of sand waves toward equilibrium for different storm conditions on a limited domain size (section 4.2). Then we show how our model performs on a much longer domain with a random initial perturbation, such that the domain length is less restrictive for the sand wave wavelength and variations in the sand wave pattern appear (section 4.3). Finally, we show the effect of intermittent storm occurrence on sand wave dynamics (section 4.4). The used parameter settings, chosen to be consistent with Campmans et al. (2017), are shown in Table 1, and an overview of simulations for the different storm processes is shown in Table 2. For clarity, we restrict to symmetrical tidal conditions, with asymmetries occurring due to wind forcing. The number of discrete points in the computations in the horizontal is $I = 64$ for the limited domain size and $I = 512$ for the longer domain size, in the vertical $J = 20$ points are used.

4.1. Comparison With Linear Stability Analysis

Our nonlinear sand wave model and the linear study by Campmans et al. (2017) are both based on the same model formulation. Hence, in the linear regime, both linear stability analysis and our nonlinear sand wave model should give the same solution. Linear stability analysis predicts exponential growth/decay and migration of sinusoidal bed shapes according to $h(x,t) = \hat{h}_{init}\exp(\omega t)\cos(k[x - c_{mig}t])$ with growth rate ω and migration rate c_{mig}, which are both functions of topographic wavenumber k and other model parameters. Therefore, to make the model results comparable, we have run the nonlinear model with a small amplitude

Table 2
Overview of Simulations, Forcing Conditions per Run and the Sand Wave Height and Migration Rates at the End of the Simulations

Figure	μ (–)	L (m)	H_{w0} (m)	T (s)	θ_{wave0} (°)	$\lvert \mathbf{U}_{wind} \rvert$ (m/s)	θ_{wind} (°)	h_{cr} (m)	h_{tr} (m)	h_{tot} (m)	c_{mig} (m/year)
6a	-	350	-	-	-	-	-	15.3	−8.5	23.7	0
6b	-	350	2	7	0	-	-	7.4	−10.1	17.5	0
6c	-	350	-	-	-	10	0	12.0	−8.1	20.1	14.5
6d	-	350	2	7	0	10	0	6.1	−6.5	12.6	34.3
7/ 8a	-	350	-	-	-	10	0	12.0	−8.1	20.1	14.5
7/ 8b	-	350	-	-	-	10	30	12.6	−8.1	20.6	11.8
7/ 8c	-	350	-	-	-	10	60	13.7	−8.4	22.1	6.1
7/ 8d	-	350	-	-	-	10	90	14.3	−8.7	22.9	0
	-	350	2	7	0	-	-	7.4	−10.1	17.5	0
Section 4.2.3	-	350	2	7	30	-	-	7.3	−10.1	17.4	0
(text only)	-	350	2	7	70	-	-	7.3	−9.6	16.9	0
	-	350	2	7	80	-	-	8.4	−8.9	17.4	0
9a	-	4,000	-	-	-	-	-	25.6	−9.5	34.0	∼0
9b	-	4,000	2	7	0	-	-	15.1	−9.6	24.7	∼0
9c	-	4,000	-	-	-	10	0	25.2	−8.8	33.9	19*
9d	-	4,000	2	7	0	10	0	14.6	−9.5	24.1	52*
6/ 10a	0	350	-	-	-	-	-	15.3	−8.5	23.7	0
10b	1/52	350	2/-	7/-	0/-	10/-	0/-	14.9	−9.0	23.9	0.3**
10c	1/12	350	2/-	7/-	0/-	10/-	0/-	13.9	−9.6	23.5	1.3**
10d	1/6	350	2/-	7/-	0/-	10/-	0/-	12.8	−9.8	22.5	2.8**
10e	1/2	350	2/-	7/-	0/-	10/-	0/-	9.4	−8.8	18.1	11.3**
10f	1	350	2	7	0	10	0	6.1	−6.5	12.6	34.3

*The migration rate corresponding with the linear line plotted in the corresponding figure. **The net long term migration rate.

white-noise seabed perturbation, and using Fourier analysis, we have computed the corresponding growth rate per wavenumber. The growth rates from both the linear stability analysis and the nonlinear model are shown in Figure 5 for three different conditions: tide only, tide + waves, and tide + wind. Both models produce the same small amplitude growth behavior, that is, the FGM properties for tide only are a wavelength of 335 m and growth rate of 0.44 1/year; for tide + waves, a wavelength of 419 m and growth rate of 0.33 1/year; and for tide + wind, a wavelength of 335 m and a growth rate of 0.45 1/year.

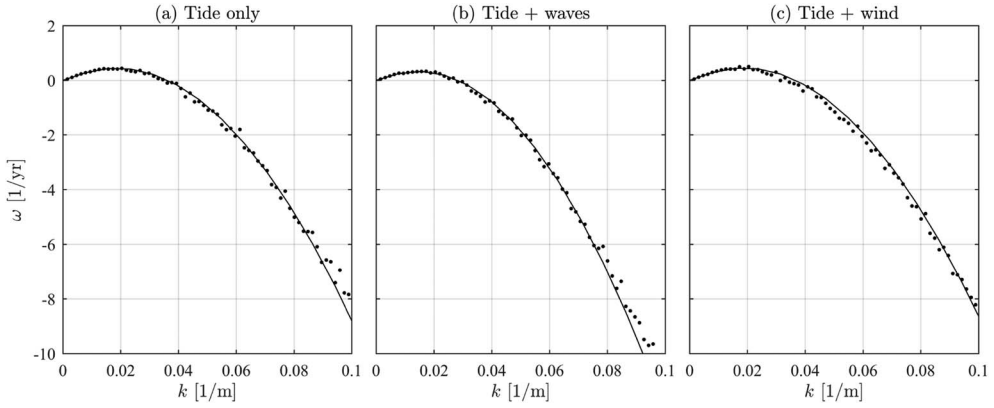

Figure 5. Comparison of our nonlinear model results (dotted) for small amplitudes with the linear stability model results (solid). Here the growth rate ω is plotted as function of the topographic wavenumber, for three conditions: (a) tide only, (b) tide + waves, and (c) tide + wind.

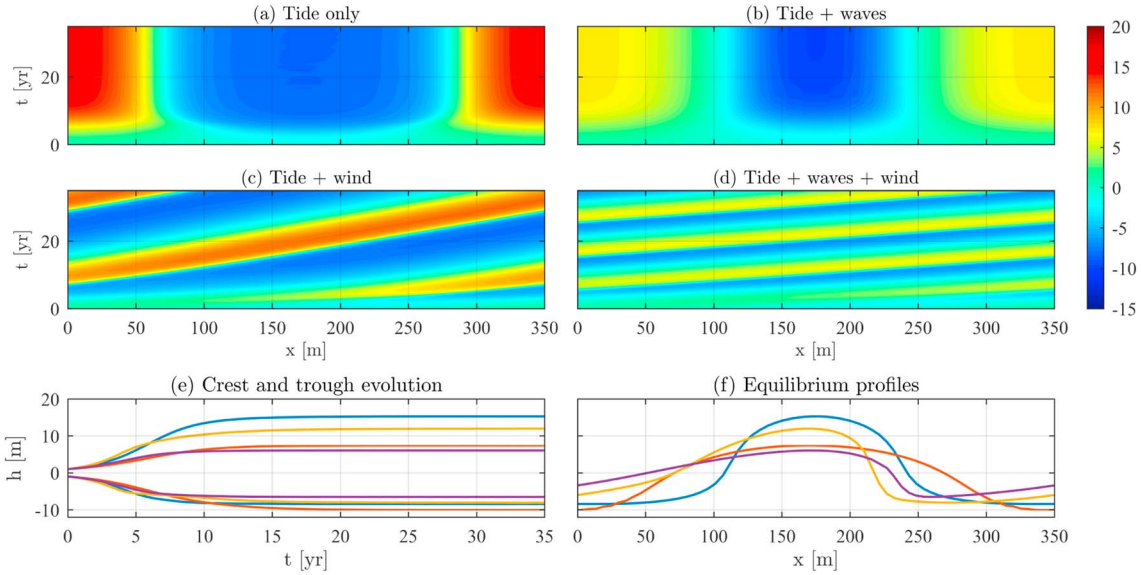

Figure 6. The seabed evolution in time and space for four different forcing conditions: (a) tide only, (b) tide + waves, (c) tide + wind, and (d) tide + waves + wind. (e) The crest and trough elevation evolution and (f) equilibrium profiles for four different forcing conditions: (blue) tide only, (red) tide + waves, (yellow) tide + wind, and (purple) tide + waves + wind. The profiles have been shifted horizontally such that the crest locations coincide. The parameter settings and forcing conditions are shown in Table 1 and 2, respectively.

4.2. Equilibrium Sand Waves With Different Forcing Conditions

On a periodic domain of 350-m length, we investigate the evolution of a 1-m amplitude sinusoidal seabed perturbation, the wavelength of which corresponds with the length of the domain. By choosing the domain length to be equal to the wavelength of the bed form, this property cannot be varied, whereas others, such as shape, height, and migration, can be investigated. The chosen domain length is a typical wavelength observed in the field and corresponds approximately to the FGM wavelength resulting from linear stability analysis for the three conditions: tide only, tide + waves and tide + wind (see Figure 5).

4.2.1. Wave and Wind Influence

Figure 6 shows the time evolution of the bed perturbation toward its fully grown state, for four different conditions: (a) tide only, (b) tide + waves, (c) tide + wind, and (d), tide + waves + wind. Here tide is a 0.5 m/s

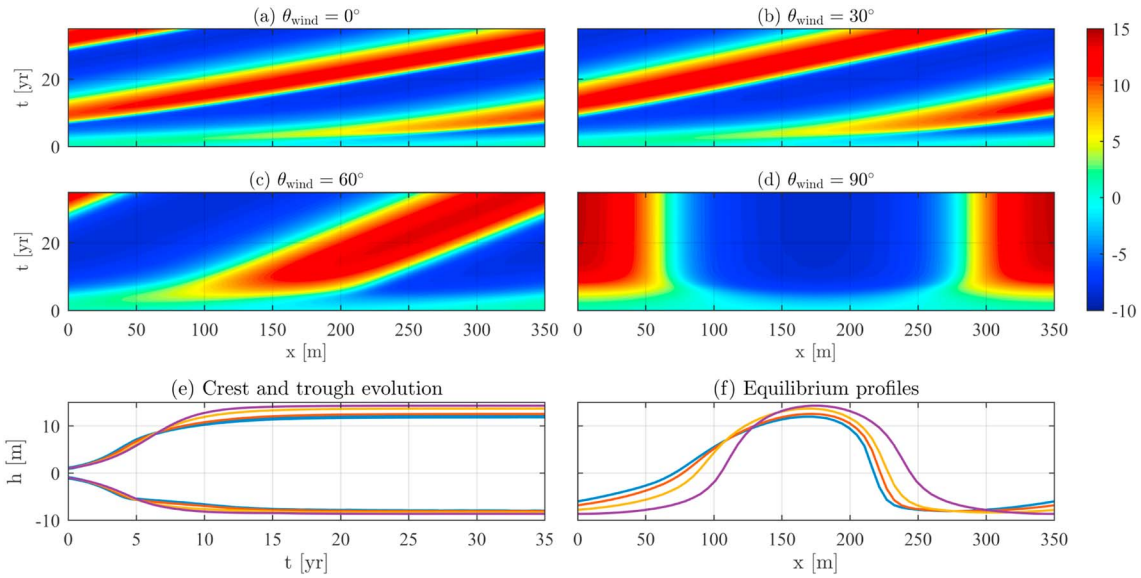

Figure 7. Same as Figure 6 but now for four wind angles in the tide + wind case: (blue) $\theta_{wind} = 0°$, (red) $\theta_{wind} = 30°$,(yellow) $\theta_{wind} = 60°$, and (purple) $\theta_{wind} = 90°$.

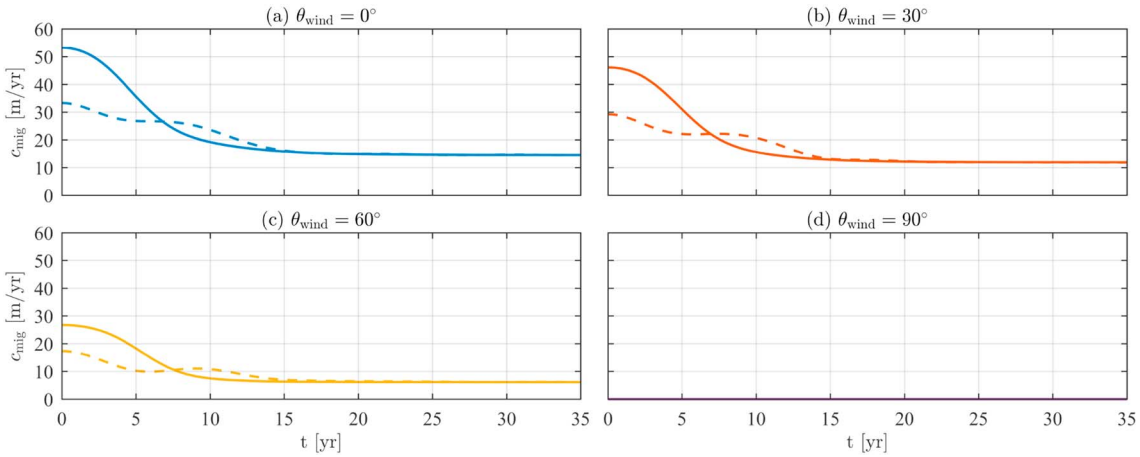

Figure 8. The migration rate of sand wave crest (solid) and trough (dashed) for four different wind angles: $\theta_{wind} = 0°$, 30°, 60°, and 90°. The parameter settings and forcing conditions are shown in Table 1 and 2, respectively.

depth-averaged symmetrical M2 constituent, waves have 2-m height and 7-s period, and wind velocity is 10 m/s, all parallel to the x directions ($\theta_{waves0} = \theta_{wind} = 0°$). The lower panels of Figure 6 show the evolution of the crest and trough elevation and the resulting (near) equilibrium profiles.

In each of the model runs, the seabed perturbation starts to grow in amplitude. Initially, the growth speed increases with increasing amplitude, but after a while, the growth speed slows down and the sand waves asymptotically approach their fully grown states. If wind waves are included, the final height is smaller. Both in the tide-only simulations and if waves are included, horizontal symmetry is preserved due to the symmetrical forcing. When adding wind-driven flow, the symmetry is broken, which leads to horizontal asymmetry and migration. The inverse of the slope dt/dx of the crest/trough lines in the x-t diagram indicates migration speed. The steady migration rates toward the end of the simulations are given in Table 2. Initially, for small heights, the migration rate is relatively fast and then decreases with increasing sand wave height, the values in the steady regime being 14.5 and 34.3 m/year. Also for wind, the final sand wave height is less than in the tide only situation. If, in addition to the tidal flow, both wind waves and wind-driven flow are present, the final sand wave height decreases even further. In that case, the migration rate of the fully grown sand waves increases as compared with the tide-only and the tide + wind cases. Note that the wave enhancement of the migration rate is twofold: (1) Linear stability analysis already showed that waves enhance migration for small amplitudes, and (2) we now find that the reduction of the sand wave height due to waves also accompanies an increase in migration speed.

4.2.2. Influence of Wind Direction

In the previous section, we have seen that wind-driven flow in the direction of the tidal flow causes sand wave migration and decreases sand wave height. In this section investigate the influence of the angle of the wind with respect to the tidal current. In Figure 7, the seabed evolution toward equilibrium profiles is shown for four simulations where a 10-m/s wind directed in four different directions with respect to the tidal flow: $\theta_{wind} = 0°, 30°, 60°$, and 90°. The model run with $\theta_{wind} = 0°$ was already shown in the previous section and is shown here again as reference. The migration rate is shown in Figure 8. Once the sand wave profile is approximately in equilibrium, the entire profile migrates at the same speed, which is 14.5, 11.8, 6.1, and 0 m/year for Figures 8a–8d, respectively. For increasing wind angle, the sand wave height increases, the migration rate decreases, and also, bed form asymmetry decreases. The decrease in migration rate is twofold: first, the wind-driven flow component in the migration direction gets smaller as the wind angle increases; and second, in section 4.2.1, we have seen that the migration rate decreases with increasing sand wave height. For wind perpendicular to the tidal flow direction, the wind-driven flow does not break the symmetry in the x direction, and therefore, the bed form does not migrate. While the seabed profile is developing, the migration rates of crest and trough are different because the profiles are becoming horizontally asymmetric. Here we should mention that the forcing conditions are no longer symmetrical in the y direction, meaning that sand wave orientation in principle no longer has to be perpendicular to the x direction. However, here we still assume the

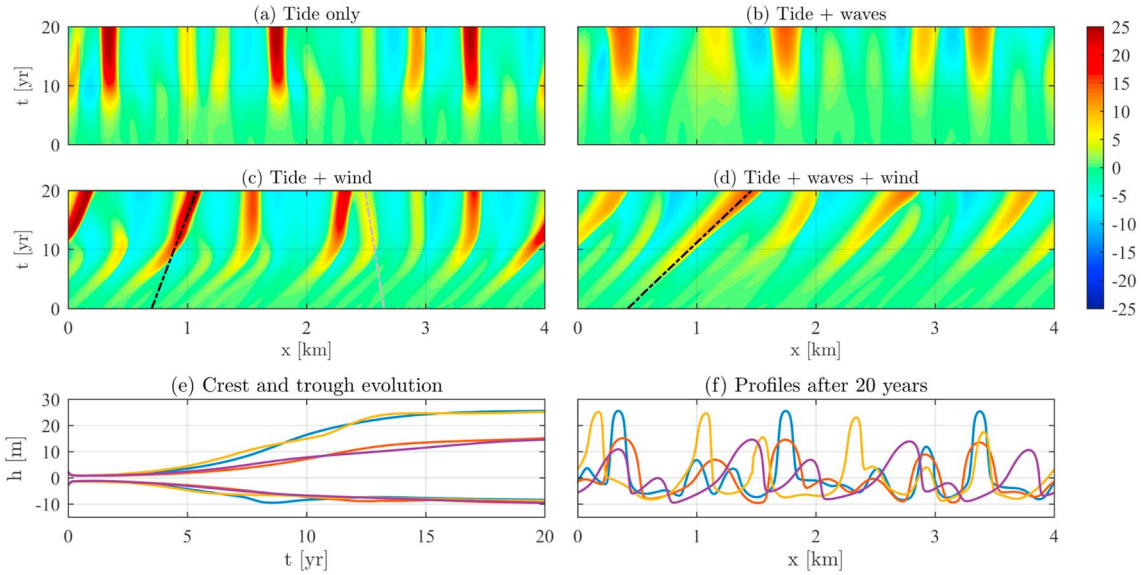

Figure 9. The evolution of the seabed for four different forcing conditions: (a) tide only, (b) tide + waves, (c) tide + wind, and (d) tide + waves + wind. The crest and trough elevation evolution (e) and the profiles after 20 years (f) are shown in the lower two panels, in which the four different forcing conditions are (blue) tide only, (red) tide + waves, (yellow) tide + wind, and (purple) tide + waves + wind. The parameter settings and forcing conditions are shown in Table 1 and 2, respectively. The dash dotted lines correspond to a constant migration speed indicated in Table 2. The gray dash dotted line (c) corresponds to a migration rate opposite to the general trend.

sand wave profile to be uniform in *y* direction. The values of the migration rates found in equilibrium, roughly satisfy a cosine relationship, that is, $c_{mig,eq}(\theta_{wind}) \approx c_{mig,eq}(0°)\cos\theta_{wind}$.

4.2.3. Influence of Wave Direction

The influence of wave direction has been investigated for four wave propagation directions $\theta_{wave0} = 0°, 30°, 70°$, and 80°. Simulations, not shown here, indicate that the evolution of the seabed is insensitive to small wave angles. For larger wave angles, the crests become slightly higher, the troughs turn out to be wider and shallower, and the sand wave height slightly increases.

4.3. Sand Wave Evolution on a Long Domain

In the previous sections, we have investigated the influence of waves and wind on a domain with a length corresponding with the wavelength of typical observed sand waves. Due to this choice, sand waves were unable to freely modify their wavelengths. By increasing the domain length to 4 km, sand waves of 350 m are now more free to modify their wavelength as they evolve, without changing the periodic boundary conditions of our model. The model is run with four forcing conditions: (a) tide only, (b) tide + waves, (c) tide + wind, and (d) tide + waves + wind (see Table 2). The initial bed profile for each of the four runs is identical: the sum of sinusoidal perturbations of all possible spatial frequencies with an equally small amplitude and a random phase shift, such that all possible modes are equally present at the start of the simulation.

The time evolution of the sand wave profiles and height is shown in Figure 9. Initially, the modes with large wave numbers rapidly decay, whereas those with lower wave numbers develop into a dynamic sand wave field. In a time period of about 5–15 years in each of the model runs, a sand wave pattern has developed which shows similarities with observed sand wave fields. The semirandom initial topography enables showing how variations in the sand wave field could develop. Initially, the FGM, predicted by linear stability analysis (Campmans et al., 2017), with a wavelength of around 330–420 m, dominates other modes. However, as time progresses, the dominant wavelength increases toward roughly 600–1,000 m. It should be noticed that the sand wave profiles after 20 years, shown in Figure 9f, are not yet in equilibrium. On time scales much longer than those plotted here, the system seems to evolve to a single bed form with a wavelength equal to the domain size. This will be further discussed in section 5.

In these simulations, we see variations in the sand wave field, where sand waves of different wavelengths are interacting with each other, causing variations in sand wave migration. The migration rate of a relatively small sand wave indicated with the gray dash dotted line in Figure 9c corresponds to a migration rate of −8

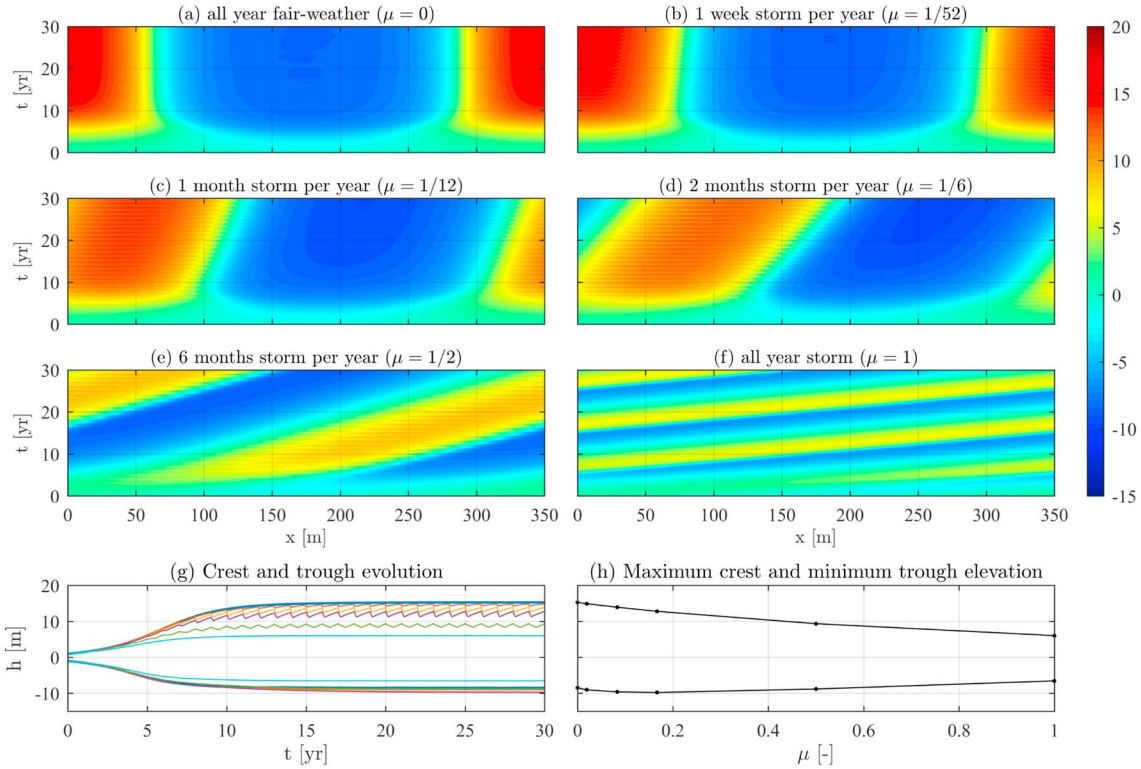

Figure 10. The evolution of the seabed for six different storm conditions: (a) all-year fair weather, (b) 1-week storm, (c) 1-month storm, (d) 2-month storm, (e) 6-month storm, and (f) all-year storm. The evolution of crest and trough elevation (g) is plotted for constant fair-weather conditions (blue), constant storm conditions (light blue), and alternating storm and fair-weather conditions: 1 week per year storm (red), 1 month per year storm (yellow), 2 months per year storm (purple), and 6 months per year storm (green). The maximum crest and minimum trough elevation are plotted against the storm ratio in the synthetic storm sequence (h). The parameter settings and forcing conditions are shown in Table 1 and 2, respectively.

m/year, while another sand wave (black dash dotted) migrates at 19 m/year. Even in the symmetrically forced model runs, shown in Figures 9a and 9b, minor migration rates in various directions can be observed due to the pattern interactions. In the model runs with wind-driven flow, large migration rates can be observed, with substantial variations in migration speed for the individual sand waves, especially when sand waves overtake each other. These sand wave interactions can result in significant seabed level changes within a relatively short timespan.

4.4. Effects of Intermittent Storms

In the previous sections, we have investigated the effect of constant wind and wave conditions on sand wave dynamics. However, in reality, storms occur intermittently. In this section we investigate the effect of a synthetic regular intermittent storm climate. Two conditions, fair weather and a storm condition, are alternated on a yearly periodic basis. The fair weather coincides with the tide only situation. The storm condition consist of 2-m high waves of 7-s period propagating parallel to the *x*axis and 10-m/s wind parallel to the *x* axis. In Figure 10, the sand wave evolution is plotted for constant fair weather, constant storm, and alternating storm and fair-weather conditions. Four storm duration intervals are shown: 1-week ($\mu = 1/52$), 1-month ($\mu = 1/12$), 2-month ($\mu = 1/6$), and 6-month storms ($\mu = 1/2$). Where μ is the ratio of the storm duration over the overall time period. The intermittent storm sequences of 1-week, 1-month, and 2-month storm conditions show migration rates of 0.3, 1.3, and 2.8 m/year, respectively, which are comparable to those reported in literature (e.g., Fenster et al., 1990; Van Dijk & Kleinhans, 2005). A clear difference in sand wave crest and trough elevation between constant fair-weather ($\mu = 0$) and constant storm ($\mu = 1$) conditions is observed. For each of the intermittent storm sequences, the trough and especially the crest show oscillating elevations, which lie in between those of the constant fair-weather and constant storm conditions. These oscillations result from the continuous adjustment toward equilibrium states that periodically switch from *high* (tide only, i.e., no waves or wind) to *low* (tide + waves + wind). Note that the crest and trough elevations of the 6-month simulation are not midway but more toward the constant storm simulation. Figure 10h shows the maximum crest height and

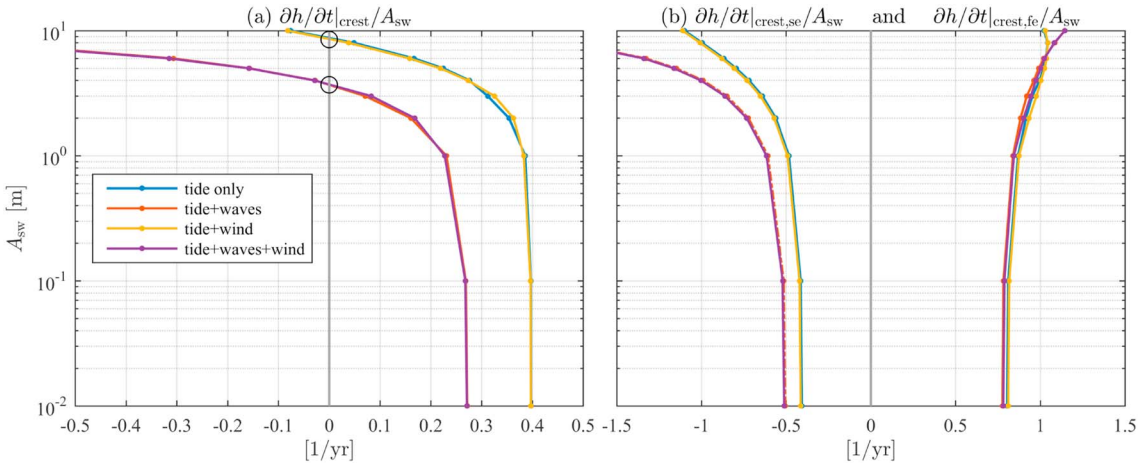

Figure 11. The divergence of sediment transport, scaled with the bed form amplitude A_{sw}, evaluated at the crest of sinusoidal bed forms as function of bed form amplitude A_{sw}. The total growth (a) is the sum of the slope-induced and flow-induced contributions (b). Four conditions have been investigated: tide only (blue), tide + waves (red), tide + wind (yellow), and tide + waves + wind (purple). The parameters and forcing conditions as in Figure 6. The zero crossings are indicated with a circle.

minimum trough depth as function of the storm duration μ. The migration rate that was obtained for the constant storm conditions is 34.3 m/year, which is large compared to field observations. By including the storms intermittently for 1 and 2 months, the obtained migration speeds are 1.3 and 2.8 m/year, respectively, which are realistic values. For these storm durations, the reduction in crest height is 9% and 16%, respectively. Longer storm periods, that is, 6 months or constant storm, reduce the crest height by 39% and 60%, respectively. This shows that even if storm conditions occur for a short period of time, their influence is still of importance.

5. Discussion

Sand wave height still seems to be overestimated in our model, especially for the tide only situation. Note that we did not calibrate our model against field observations. Calibration with, for instance, the slope correction parameter could result in more realistic sand wave heights. However, our goal is to investigate whether storms could be a mechanism which is responsible for lowering sand wave heights.

The mechanism that is responsible for waves to reduce the sand wave growth rate can be explained by examining the bed load transport terms in equation (25). The magnitude of transport is nonlinearly dependent on the shear stress magnitude. This nonlinearity in sediment transport results in a net increase in transport due to increased wave stirring, and since the slope-induced transport is always directed downslope, this term reduces the growth rate.

To clarify the saturation mechanism and the influence of waves and wind on the equilibrium height, we have conducted another set of simulations. Herein we have computed for sinusoidally shaped initial topographies of various amplitudes, A_{sw}, the rate of change of the crest height $\partial h/\partial t|_{\text{crest}}$ (after spin-up of the flow), divided by amplitude A_{sw}, as a function of the amplitude A_{sw}. Note that the rate of change divided by amplitude is equivalent to the growth rate in linear stability analysis and is thus expected to be constant for small amplitudes and through nonlinear effects changes for larger amplitudes. Distinguishing the two contributions (flow-induced and slope-induced) introduced in equation (25), we have compared the four types of forcing conditions: tide only, tide + waves, tide + wind, and tide + waves + wind. Importantly, by investigating a sinusoidal sand wave shape for all amplitudes, we avoid indirect effects through the evolution of the sand wave shape (which would be different for each forcing condition, thus obscuring comparison and interpretation). The result, shown in Figure 11, demonstrates the following:

- Nonlinear effects amplify the relative contributions due to flow and slope for increasing A_{sw} (otherwise all lines in Figure 11 would be vertical).
- This amplification is stronger for the slope-induced than for the flow-induced contribution, which explains the occurrence of an equilibrium. Note that this is not a formal equilibrium, because nonlinear effects tend to change the shape of the bed form.

- Finally, waves enhance the slope-induced contribution, which causes the equilibrium amplitude to shift to a lower value. Note that, restricting to the linear regime (A_{sw} small compared to mean water depth), this enhancement was already identified by Campmans et al. (2017).

Storm events occur randomly and have limited duration, while in our model, the storm processes are mostly modeled steady. Therefore, the model results before section 4.4 do not resemble the effect of a single storm event but rather the theoretical equilibrium state to which the system would tend during a storm. Therefore, to gain insight in intermittent storm processes, one storm condition has been alternated with fair weather. Even when storms only occur for a short period of time, they have a relatively large effect on the behavior of sand waves (Figure 10). This observation emphasizes the importance of storm effects on sand wave dynamics.

Our model shows, in agreement with linear stability analysis, that wind-driven flow is able to cause sand wave migration. Since the sand wave shape becomes horizontally asymmetric, the migration rate is initially different for the crest and trough. As the sand wave height increases, the migration rate decreases, which is also obtained from data analysis (Knaapen, 2005) and is observed in modeling other morphological features, such as nearshore sand bars (Garnier et al., 2006). This suggests that migration rates predicted by linear stability analysis are expected to be higher than those of fully grown sand waves. Although sand wave migration speed decreases with increasing height, in long domain simulations with an initial random bed, higher sand waves are found to overtake smaller sand waves. This seems counterintuitive. The hydrodynamic conditions around a smaller sand wave close to an approaching higher sand wave are influenced such that the higher sand wave migrates faster than the lower sand wave. Neighboring sand waves thus affect each others growth and migration behavior. Even for symmetrical flow conditions, that is, tide only and tide + waves, small migration rates can be observed when neighboring sand waves attract or repel each other. For tide + wind conditions, smaller sand waves even migrate in the direction opposing the domain-averaged residual flow, showing that sand waves strongly interact with each other. Finally, note that variations in wind direction and intensity might cause the average migration rate to be significantly smaller than the values obtained here for a single wind condition.

Sand wave models, including the present one, still lack a mechanism that keeps sand waves from tending toward very long wavelengths. This is a fundamental problem in this type of morphodynamic model, as this is also observed for other bed features such as sand banks. We have limited the wavelength artificially by using a limited domain size, in order to investigate the influence of storm effects on sand wave dynamics. Mechanisms that might limit the wavelength may be found in horizontal variations of the tidal wave (we assume horizontal uniformity of the forcing on the length scale of the sand waves). Also, interactions with other bed forms such as sand banks or mega ripples might be of importance. Stochastic variations in currents and waves might also affect the preferred wavelength.

6. Conclusion

We have developed an idealized nonlinear sand wave model that is able to simulate sand wave evolution from an initial small perturbation toward a fully developed equilibrium state. Using this model, we are able to investigate storm effects on sand wave evolution. The modeled equilibrium sand waves in tide + wave + wind conditions become about 15 m high and 600–1,000 m in wavelength, migrate at about 50 m/year, and are formed in roughly 10 years. Our most important results are that wind waves and, to a lesser degree, wind-driven flow tend to decrease sand wave height, and wind-driven flow causes asymmetry and migration. The wave-induced reduction in sand wave height is explained from the balance between flow-induced and slope-induced sediment transport contributions. Wind waves enhance the slope-induced sediment transport, leading to a reduction in equilibrium height. Waves as modeled here do not induce migration but enhance sand wave migration due to other processes, such as wind-driven flow or tidal asymmetry (the latter not being included in this contribution). The direction of wind-driven flow affects horizontal asymmetry, height reduction, and migration effects. Wind parallel to the tidal current results in the largest asymmetry, migration, and height reduction, whereas perpendicular wind results in symmetrical sand waves that do not migrate and causes the smallest reduction in height. The wave angle appears to be of less importance; only for wave angles close to 90°, the wave angle seems to have an influence. Finally, we show that short periods of storms can already have significant effects on sand wave height and lead to realistic migration rates.

Appendix A: Spatial Hydrodynamic Discretization

Here we describe how the transformed model equations have been discretized. The transformed continuity equation (19) is discretized by

$$\frac{\tilde{u}_{i+1,j} - \tilde{u}_{i,j}}{\Delta\tilde{x}} + \frac{\tilde{w}_{i,j} - \tilde{w}_{i,j-1}}{\Delta\tilde{z}} = 0. \tag{A1}$$

The transformed momentum equations (20) are spatially discretized by

$$\begin{aligned}\frac{\partial\tilde{u}_{i,j}}{\partial t} &+ \frac{\tilde{\mathcal{F}}_{u,x,i+\frac{1}{2},j} - \tilde{\mathcal{F}}_{u,x,i-\frac{1}{2},j}}{\Delta\tilde{x}} + \frac{\tilde{\mathcal{F}}_{u,z,i,j+\frac{1}{2}} - \tilde{\mathcal{F}}_{u,z,i,j-\frac{1}{2}}}{\Delta\tilde{z}} \\ &+ \frac{g}{\xi_{i-\frac{1}{2}}}\frac{\tilde{\zeta}_i - \tilde{\zeta}_{i-1}}{\Delta\tilde{x}} - \frac{\tilde{F}_x}{\xi_{i-\frac{1}{2}}} = 0,\end{aligned} \tag{A2}$$

$$\begin{aligned}\frac{\partial\tilde{v}_{i,j}}{\partial t} &+ \frac{\tilde{\mathcal{F}}_{v,x,i+\frac{1}{2},j} - \tilde{\mathcal{F}}_{v,x,i-\frac{1}{2},j}}{\Delta\tilde{x}} + \frac{\tilde{\mathcal{F}}_{v,z,i,j+\frac{1}{2}} - \tilde{\mathcal{F}}_{v,z,i,j-\frac{1}{2}}}{\Delta\tilde{z}} \\ &- \frac{\tilde{F}_y}{\xi_{i-\frac{1}{2}}} = 0.\end{aligned} \tag{A3}$$

Here we use linear interpolation to evaluate $\xi_{i-\frac{1}{2}}$ according to $\xi_{i-\frac{1}{2}} = \frac{1}{2}(\xi_{i-1} + \xi_i)$. The flux terms, as presented in equation (22), are discretized by

$$\begin{aligned}\tilde{\mathcal{F}}_{u,x,i+\frac{1}{2},j} &= \xi_i \tilde{u}^{*2}_{i+\frac{1}{2},j} \\ \tilde{\mathcal{F}}_{v,x,i+\frac{1}{2},j} &= \xi_i \tilde{v}^{*}_{i+\frac{1}{2},j} \tilde{u}^{*}_{i+\frac{1}{2},j} \\ \tilde{\mathcal{F}}_{u,z,i,j+\frac{1}{2}} &= \xi_{i-\frac{1}{2}} \tilde{u}^{*}_{i,j+\frac{1}{2}} \tilde{w}_{i-\frac{1}{2},j} - \xi^2_{i-\frac{1}{2}} A_v \frac{\tilde{u}_{i,j+1} - \tilde{u}_{i,j}}{\Delta\tilde{z}} \\ \tilde{\mathcal{F}}_{v,z,i,j+\frac{1}{2}} &= \xi_{i-\frac{1}{2}} \tilde{v}^{*}_{i,j+\frac{1}{2}} \tilde{w}_{i-\frac{1}{2},j} - \xi^2_{i-\frac{1}{2}} A_v \frac{\tilde{v}_{i,j+1} - \tilde{v}_{i,j}}{\Delta\tilde{z}}.\end{aligned} \tag{A4}$$

Here linear interpolation is used to evaluate the vertical velocities that are required in between grid points, $\tilde{w}_{i-\frac{1}{2},j} = \frac{1}{2}\left(\tilde{w}_{i-1,j} + \tilde{w}_{i,j}\right)$. The state variables, $\tilde{\mathbf{u}}^*_{h,i,j}$, which are required at the intergrid points, are computed using linear reconstruction including a so-called limiter function which improves the stability properties of the scheme (Van Leer, 1979). For instance, for the horizontal momentum flux, the horizontal velocities on the left and right side of the interface are reconstructed using

$$\begin{aligned}\tilde{u}^L_{i+\frac{1}{2},j} &= \tilde{u}_{i,j} + \frac{1}{2}\phi(r_{i,j})(\tilde{u}_{i+1,j} - \tilde{u}_{i,j}) \\ \tilde{u}^R_{i-\frac{1}{2},j} &= \tilde{u}_{i,j} - \frac{1}{2}\phi(r_{i,j})(\tilde{u}_{i+1,j} - \tilde{u}_{i,j}).\end{aligned} \tag{A5}$$

Here $\phi(r)$ is a limiter function, for which we choose the symmetric superbee limiter (Roe, 1986), given by

$$\phi(r) = \max(0, \max(\min(1, 2r), \min(2, r))), \tag{A6}$$

where r is the ratio between the forward and backward difference, for example, the horizontal difference ratio $r_{i,j}$ in equation (A5) is given by

$$r_{i,j} = \frac{\tilde{u}_{i,j} - \tilde{u}_{i-1,j}}{\tilde{u}_{i+1,j} - \tilde{u}_{i,j}}. \tag{A7}$$

Finally, the interface states used to evaluate the fluxes are determined by approximately solving the Riemann problem at each of the interface using the two states on either side of the interface, for example,

$$\tilde{u}^*_{i+\frac{1}{2},j} = \begin{cases} \tilde{u}^L_{i+\frac{1}{2},j} & \text{if} \quad \tilde{u}^L_{i+\frac{1}{2},j} > \tilde{u}^R_{i+\frac{1}{2},j} \quad \text{and} \quad s > 0 \\ \tilde{u}^R_{i+\frac{1}{2},j} & \text{if} \quad \tilde{u}^L_{i+\frac{1}{2},j} > \tilde{u}^R_{i+\frac{1}{2},j} \quad \text{and} \quad s < 0 \\ \tilde{u}^L_{i+\frac{1}{2},j} & \text{if} \quad \tilde{u}^L_{i+\frac{1}{2},j} < \tilde{u}^R_{i+\frac{1}{2},j} \quad \text{and} \quad \tilde{u}^L_{i+\frac{1}{2},j} > 0 \\ \tilde{u}^R_{i+\frac{1}{2},j} & \text{if} \quad \tilde{u}^L_{i+\frac{1}{2},j} < \tilde{u}^R_{i+\frac{1}{2},j} \quad \text{and} \quad \tilde{u}^R_{i+\frac{1}{2},j} < 0 \\ 0 & \text{if} \quad \tilde{u}^R_{i+\frac{1}{2},j} > 0 > \tilde{u}^L_{i+\frac{1}{2},j}, \end{cases} \tag{A8}$$

where s is the shock speed given by

$$s = \frac{1}{2}(\tilde{u}^L_{i+\frac{1}{2},j} + \tilde{u}^R_{i+\frac{1}{2},j}). \tag{A9}$$

The boundary conditions are implemented using ghost cells, given by

$$\begin{aligned} &\tilde{w}_{i,J} = 0, && \tilde{\mathbf{u}}^G_{\mathrm{h},i,J+1} = \tilde{\mathbf{u}}_{\mathrm{h},i,J} + \frac{\Delta\tilde{z}\boldsymbol{\tau}_{\mathrm{wind}}}{A_\mathrm{v}\rho\xi^2_{i-\frac{1}{2}}},\\ &\tilde{w}_{i,0} = 0, && \tilde{\mathbf{u}}^G_{\mathrm{h},i,0} = \tilde{\mathbf{u}}_{\mathrm{h},i,1}\frac{(\xi_{i-1}+\xi_i)A_\mathrm{v} - S\Delta\tilde{z}}{(\xi_{i-1}+\xi_i)A_\mathrm{v} + S\Delta\tilde{z}},\\ &\tilde{\mathbf{u}}^G_{\mathrm{h},I+1,j} = \tilde{\mathbf{u}}_{\mathrm{h},1,j}, && \tilde{\zeta}^G_0 = \tilde{\zeta}_I, \end{aligned} \tag{A10}$$

where ghost values are denoted by superscript G, and note that we start indexing with 1 for interior cells. The horizontal domain bounds are treated as periodic, that is, the right most cells are seen as the left neighbors of the left most cell in the domain and vice versa. The discrete bed shear stresses are given by

$$\boldsymbol{\tau}_i = \frac{\rho S}{4}(\xi_{i-1}+\xi_i)(\tilde{\mathbf{u}}^G_{\mathrm{h},i,0} + \tilde{\mathbf{u}}_{\mathrm{h},i,1}). \tag{A11}$$

Acknowledgments
This work is part of the research programme SMARTSEA with project number 13275, which is (partly) financed by the Netherlands Organisation for Scientific Research (NWO). The numerical code cannot be made available at submission (a condition by the funder), but the first author will facilitate code use for verification purposes should anybody seek this. We thank Daniel Calvete Manrique for his support and for facilitating a stay at Universitat Politècnica de Catalunya, Barcelona, Spain. We thank anonymous reviewers for their comments.

References

Besio, G., Blondeaux, P., Brocchini, M., Hulscher, S. J. M. H., Idier, D., Knaapen, M. A. F., et al. (2008). The morphodynamics of tidal sand waves: A model overview. *Coastal Engineering*, *55*(7), 657–670.

Besio, G., Blondeaux, P., Brocchini, M., & Vittori, G. (2004). On the modeling of sand wave migration. *Journal of Geophysical Research*, *109*, C04018. https://doi.org/10.1029/2002JC001622

Besio, G., Blondeaux, P., & Vittori, G. (2006). On the formation of sand waves and sand banks. *Journal of Fluid Mechanics*, *557*, 1–27.

Blondeaux, P., & Vittori, G. (2005a). Flow and sediment transport induced by tide propagation: 1. The flat bottom case. *Journal of Geophysical Research*, *110*, C07020. https://doi.org/10.1029/2004JC002532

Blondeaux, P., & Vittori, G. (2005b). Flow and sediment transport induced by tide propagation: 2. The wavy bottom case. *Journal of Geophysical Research*, *110*, C08003. https://doi.org/10.1029/2004JC002545

Borsje, B. W., Kranenburg, W. M., Roos, P. C., Matthieu, J., & Hulscher, S. J. M. H. (2014). The role of suspended load transport in the occurrence of tidal sand waves. *Journal of Geophysical Research: Earth Surface*, *119*, 701–716. https://doi.org/10.1002/2013JF002828

Borsje, B. W., Roos, P. C., Kranenburg, W. M., & Hulscher, S. J. M. H. (2013). Modeling tidal sand wave formation in a numerical shallow water model: The role of turbulence formulation. *Continental Shelf Research*, *60*, 17–27.

Bowden, K. F., Fairbairn, L. A., & Hughes, P. (1959). The distribution of shearing stresses in a tidal current. *Geophysical Journal International*, *2*(4), 288–305.

Campmans, G. H. P., Roos, P. C., de Vriend, H. J., & Hulscher, S. J. M. H. (2017). Modeling the influence of storms on sand wave formation: A linear stability approach. *Continental Shelf Research*, *137*, 103–116. https://doi.org/10.1016/j.csr.2017.02.002

Damen, J. M., van Dijk, T. A. G. P., & Hulscher, S. J. M. H. (2018). Spatially varying environmental properties controlling observed sand wave morphology. *Journal of Geophysical Research: Earth Surface*, *123*, 262–280. https://doi.org/10.1002/2017JF004322

Dodd, N., Blondeaux, P., Calvete, D., De Swart, H. E., Falqués, A., Hulscher, S. J. M. H., et al. (2003). Understanding coastal morphodynamics using stability methods. *Journal of Coastal Research*, *19*, 849–865.

Dorst, L. L., Roos, P. C., & Hulscher, S. J. M. H. (2011). Spatial differences in sand wave dynamics between the Amsterdam and the Rotterdam region in the Southern North Sea. *Continental Shelf Research*, *31*(10), 1096–1105.

Fenster, M. S., Fitzgerald, D. M., Bohlen, W. F., Lewis, R. S., & Baldwin, C. T. (1990). Stability of giant sand waves in eastern Long Island Sound, USA. *Marine Geology*, *91*(3), 207–225.

Garnier, R., Calvete, D., Falqués, A., & Caballeria, M. (2006). Generation and nonlinear evolution of shore-oblique/transverse sand bars. *Journal of Fluid Mechanics*, *567*, 327–360.

Harris, P. T. (1989). Sandwave movement under tidal and wind-driven currents in a shallow marine environment: Adolphus Channel, northeastern Australia. *Continental Shelf Research*, *9*(11), 981–1002.

Houthuys, R., Trentesaux, A., & De Wolf, P. (1994). Storm influences on a tidal sandbank's surface (Middelkerke Bank, southern North Sea). *Marine Geology*, *121*(1), 23–41.

Hulscher, S. J. M. H. (1996). Tidal-induced large-scale regular bed form patterns in a three-dimensional shallow water model. *Journal of Geophysical Research*, *101*(C9), 20,727–20,744.

Hulscher, S. J. M. H., & van den Brink, G. M. (2001). Comparison between predicted and observed sand waves and sand banks in the North Sea. *Journal of Geophysical Research*, *106*(C5), 9327–9338.

Knaapen, M. A. F. (2005). Sandwave migration predictor based on shape information. *Journal of Geophysical Research*, *110*, F04S11. https://doi.org/10.1029/2004JF000195

Le Bot, S., Trentesaux, A., Garlan, T., Berne, S., & Chamley, H. (2000). Influence des tempêtes sur la mobilité des dunes tidales dans le détroit du Pas-de-Calais. *Oceanologica Acta*, *23*(2), 129–141.

Maas, L. R. M., & van Haren, J. J. M. (1987). Observations on the vertical structure of tidal and inertial currents in the central north sea. *Journal of Marine Research*, *45*(2), 293–318. https://doi.org/10.1357/002224087788401106

Makin, V. K., Kudryavtsev, V. N., & Mastenbroek, C. (1995). Drag of the sea surface. *Boundary-Layer Meteorology*, *73*(1–2), 159–182.

McCave, I. N. (1971). Sand waves in the North Sea off the coast of Holland. *Marine Geology*, *10*(3), 199–225.

Mei, C. C. (1989). *The Applied Dynamics of Ocean Surface Waves* (Vol. 2, pp. 61). Singapore: World Scientific Publishing Co. Pte. Ltd.

Németh, A. A., Hulscher, S. J. M. H., & de Vriend, H. J. (2002). Modelling sand wave migration in shallow shelf seas. *Continental Shelf Research*, *22*(18), 2795–2806.

Németh, A. A., Hulscher, S. J. M. H., & Van Damme, R. M. J. (2007). Modelling offshore sand wave evolution. *Continental Shelf Research*, *27*(5), 713–728.
Nielsen, P. (1992). *Coastal Bottom Boundary Layers and Sediment Transport* (Vol. 4). River Edge, NJ: World Scientific.
Roe, P. L. (1986). Characteristic-based schemes for the Euler equations. *Annual Review of Fluid Mechanics*, *18*(1), 337–365.
Roos, P. C., Hulscher, S., Van Der Meer, F., Van Dijk, T. A. G. P., Wientjes, I. G. M., & van den Berg, J. (2007). Grain size sorting over offshore sand-waves: Observations and modelling. In C. M. Dohmen-Janssen & S. J. M. H. Hulscher (Eds.), *River, Coastal and Estuarine Morphodynamics, RCEM 2007, 17–21 September 2007, Enschede, The Netherlands, Vol I* (pp. 649–656). London: Taylor & Francis.
Sterlini, F., Hulscher, S. J. M. H., & Hanes, D. M. (2009). Simulating and understanding sand wave variation: A case study of the golden gate sand waves. *Journal of Geophysical Research*, *114*, F02007. https://doi.org/10.1029/2008JF000999
Terwindt, J. H. J. (1971). Sand waves in the Southern Bight of the North Sea. *Marine Geology*, *10*(1), 51–67.
Van Dijk, T. A. G. P., & Kleinhans, M. G. (2005). Processes controlling the dynamics of compound sand waves in the North Sea, Netherlands. *Journal of Geophysical Research*, *110*, F04S10. https://doi.org/10.1029/2004JF000173
Van Leer, B. (1979). Towards the ultimate conservative difference scheme. V. A second-order sequel to Godunov's method. *Journal of Computational Physics*, *32*, 101–136.
Van Oyen, T., & Blondeaux, P. (2009). Grain sorting effects on the formation of tidal sand waves. *Journal of Fluid Mechanics*, *629*, 311–342.
Van Rijn, L. C. (1993). *Principles of Sediment Transport in Rivers, Estuaries and Coastal Seas* (Vol. 1006). Amsterdam: Aqua publications.
Van den Berg, J., Sterlini, F., Hulscher, S. J. M. H., & Van Damme, R. M. J. (2012). Non-linear process based modelling of offshore sand waves. *Continental Shelf Research*, *37*, 26–35.